Computer Aided Surgery, 2004; 9(5): 203–214

Taylor & Francis
Taylor & Francis Group

BIOMEDICAL PAPER

Development of a camera model and calibration procedure for oblique-viewing endoscopes

TETSUZO YAMAGUCHI[1], MASAHIKO NAKAMOTO[1], YOSHINOBU SATO[1], KOZO KONISHI[3], MAKOTO HASHIZUME[3], NOBUHIKO SUGANO[2], HIDEKI YOSHIKAWA[2], & SHINICHI TAMURA[1]

[1]*Division of Interdisciplinary Image Analysis and* [2]*Department of Orthopaedic Surgery, Osaka University Graduate School of Medicine, Osaka, Japan, and* [3]*Kyushu University Graduate School of Medicine, Fukuoka, Japan*

(Received 20 September 2004)

Abstract
Oblique-viewing endoscopes (oblique scopes) are widely used in medical practice. They are essential for certain procedures such as laparoscopy, arthroscopy and sinus endoscopy. In an oblique scope the viewing directions are changeable by rotating the scope cylinder. Although a camera calibration method is necessary to apply augmented reality technologies to oblique endoscopic procedures, no method for oblique scope calibration has yet been developed. In the present paper, we formulate a camera model and a calibration procedure for oblique scopes. In the calibration procedure, Tsai's calibration is performed at zero rotation of the scope cylinder, then the variation of the external camera parameters corresponding to the rotation of the scope cylinder is modeled and estimated as a function of the rotation angle. Accurate estimation of the rotational axis is included in the procedure. The accuracy of this estimation was demonstrated to have a significant effect on overall calibration accuracy in the experimental evaluation, especially with large rotation angles. The projection error in the image plane was approximately two pixels. The proposed method was shown to be clinically applicable.

Keywords: *Oblique scope, camera calibration, augmented reality, computer-assisted surgery, laparoscope, arthroscope*

Introduction

As a minimally invasive procedure, endoscopic surgery has become common in recent years. When rigid scopes are used, the movements of the endoscope can be tracked by a 3D position sensor attached to the camera head outside the cavity. Since endoscopic surgery is essentially a monitor-based operation, conventional monitor-based augmented reality (AR) technologies may be combined straightforwardly with rigid scope tracking without the need for special display devices or 3D glasses [1–6]. Several AR systems for rigid scopes including microscopes have already been used clinically. These systems accurately superimpose virtual and real endoscopic images. Previous studies have investigated additional parameters for endoscopic camera calibration other than those used in the conventional method of Tsai [7], and the correction of distortion caused by wide-angle lenses is often incorporated [5, 8–11]. Moreover, the zoom and focus parameters have been examined [12,13] and applied to microscopic camera calibration [14]. The zoom and focus parameters are dynamically changeable during the endoscopic procedures, while the distortion parameters are static.

There are two types of rigid endoscopes: forward-viewing endoscopes (hereafter called *forward scopes*), and oblique- or side-viewing endoscopes (hereafter

Correspondence: Yoshinobu Sato, Division of Interdisciplinary Image Analysis, Osaka University Graduate School of Medicine, Room D11, 2-2 Yamada-oka, Suita, Osaka 565-0871, Japan. Tel: +81-6-6879-3562. Fax: +81-6-6879-3569. E-mail: yoshi@image.med.osaka-u.ac.jp
This paper is based on research presented at the 6th International Conference on Medical Image Computing and Computer-Assisted Intervention (MICCAI), Montreal, Canada, November 2003.

ISSN 1092-9088 print/ISSN 1097-0150 online
DOI: 10.1080/10929080500163505

called *oblique scopes*). Because the range of movement of the scope cylinder is considerably restricted due to the fixed entry point and constriction of the cavities, it is often difficult to observe a target object from the desired viewing directions using forward scopes in which the viewing direction is aligned and fixed to the axis of the scope cylinder. Recently, oblique endoscopes have been widely used to overcome this problem. In oblique scopes, the viewing direction has a tilt (30°, for example) from the axial direction of the scope cylinder that is changeable by rotating the scope cylinder around the cylinder axis without changing the position and orientation of the camera head. Thus, oblique scopes are more advantageous than forward scopes due to their much wider variety of viewing directions, attained by rotation of the scope cylinder. To our knowledge, no camera model of oblique scopes has been developed to date, despite the fact that oblique scopes are widely used in clinical practice and are even essential for certain procedures such as laparoscopy, arthroscopy, and sinus endoscopy.

In this paper, we describe the development of a camera calibration method for oblique scopes and its application to an oblique-viewing endoscopic AR system. A preliminary report on this work has already been published [15]. While lens distortion, zoom and focus parameters are involved in the modification of the internal parameters in Tsai's camera model, the rotation parameter of the scope cylinder in oblique scopes is related to the external parameters. This rotation parameter is dynamically changeable during endoscopic procedures, similar to the zoom and focus parameters. We measure the rotation parameter of the scope cylinder using a rotary encoder attached to the camera head. The problem is formulated as determining the optical ray in the physical space corresponding to each pixel in the endoscopic image, given the rotation of the scope cylinder as measured by the rotary encoder, as well as the position and orientation of the camera head as measured by a 3D position sensor. The particular purpose of the oblique scope calibration is to find the systematic relationship between the rotation of the scope cylinder and the external parameters in Tsai's model. The problems addressed in this paper may be summarized as follows: (1) development of a camera model for oblique scopes by describing the external parameters as functions of the rotation of the scope cylinder and some system parameters; and (2) formulation of a calibration procedure for estimating unknown system parameters in the functions.

The structure of this paper is as follows. In the next section we give an overview of AR systems for oblique scopes, then describe the camera model of oblique scopes and its calibration method. In the subsequent section we describe experiments for evaluating the accuracy of the methods under various conditions, and clarify the guidelines for both efficient and accurate calibration. In the final section we discuss the work and indicate directions of future research.

Methods

Overview of oblique-viewing endoscope

The features of an oblique scope in comparison with a forward scope are illustrated in Figure 1. A rigid scope is characterized by its rigid scope cylinder. The difference in appearance between oblique and forward scopes is observed at the tips of their scope cylinders. As shown in Figure 1a, the viewing direction of a forward endoscope is aligned with the axis of the scope cylinder, while an oblique scope has a tilt away from this axis and its viewing direction is changeable by rotating the scope cylinder around the axis. Figures 1c and 1d present images of a world map on a cylindrical inner wall acquired by real forward and oblique scopes, respectively, at the positions shown in Figure 1b. As demonstrated in Figure 1d, oblique endoscopic images are changed by rotating the scope cylinder, and high-latitude regions of the map on the inner wall are much more clearly observed than in the view obtained through a forward scope.

Augmented reality system for oblique-viewing endoscope

Figure 2 shows a basic system for realizing oblique-viewing endoscopic augmented reality visualization. We attach additional apparatus to measure the pose of the camera head and the rotation of the scope cylinder. A rigid body with optical markers is attached to the camera head for measuring its 6D pose parameters using an optical tracker, and the rotary encoder is geared to the scope cylinder for measuring its rotation parameter. Let T_{tr} represent rigid transformation from 3D coordinates in the optical tracker coordinate system S_t to those in the rigid body coordinate system S_r attached to the camera head. To ensure that the system generates rendering images of a 3D image data set as virtual oblique endoscopic images superimposed on real ones, the following transformations must be available in addition to T_{tr}:

- Rigid transformation T_{dt} from 3D coordinates in the 3D image coordinate system S_d to those in the tracker coordinate system S_t.
- Rigid transformation T_{rc} from 3D coordinates in the rigid body coordinate system S_r attached to the endscope to those in the camera coordinate system S_c.
- Projection transformation M_{ci} from 3D coordinates in the camera coordinate system S_c to 2D coordinates in the projected image coordinate system.

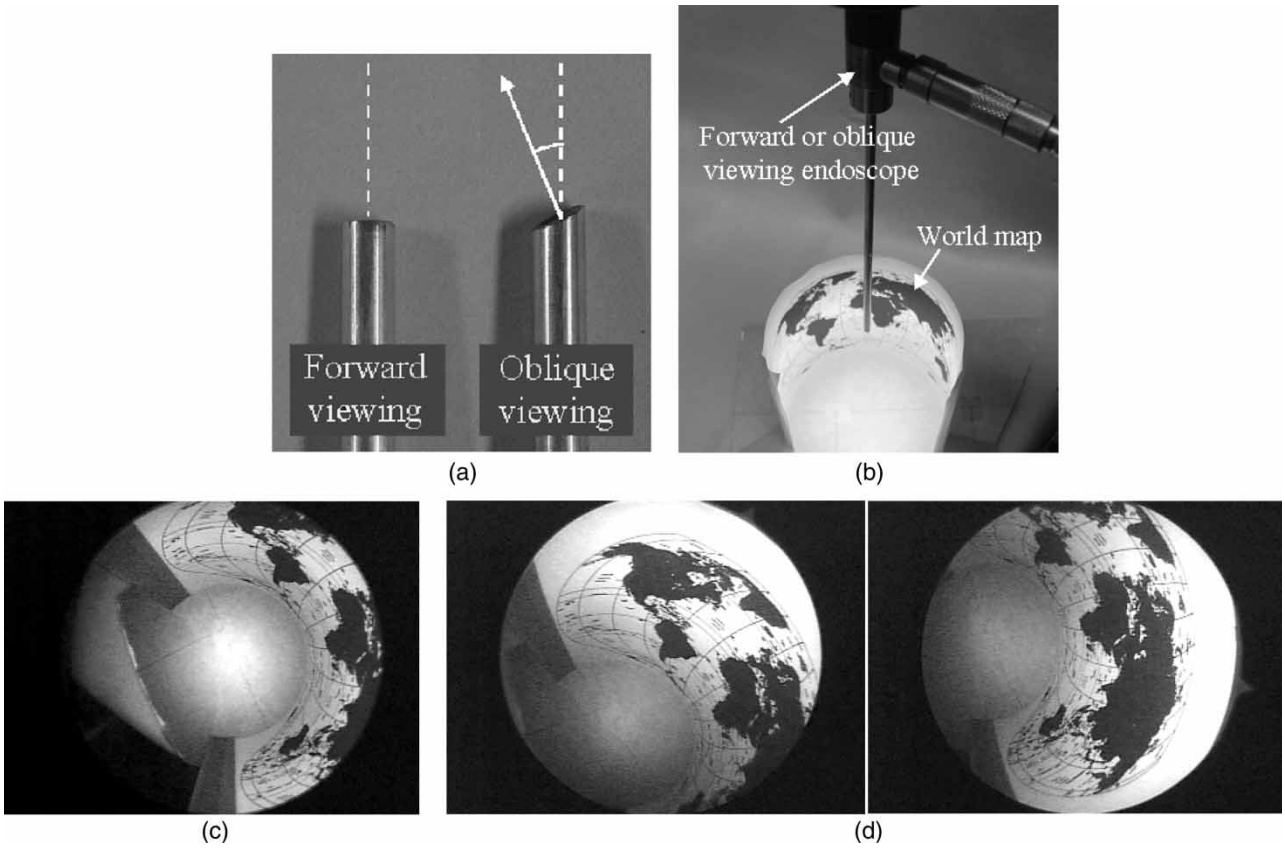

Figure 1. Comparison between forward-viewing and oblique-viewing endoscopes. (a) Tips of scope cylinders of forward and oblique viewing endoscopes. (b) Set-up for acquisition of endoscopic images. (c) Forward-viewing endoscopic image acquired using the set-up shown in (b). (d) Oblique-viewing endoscopic images with $\theta = 0^\circ$ (left) and $\theta = 60^\circ$ (right).

Typical examples of the 3D image data set are preoperative CT/MR data and intraoperative ultrasound data. Using the above transformations, the projection from homogeneous coordinates $\mathbf{p}_d$ in the 3D image data to homogeneous coordinates $\mathbf{i}_c$ in the 2D oblique-scope image is written as

$$s\mathbf{i}_c = \mathbf{p}_d T_{dt} T_{tr} T_{rc} M_{ci}, \tag{1}$$

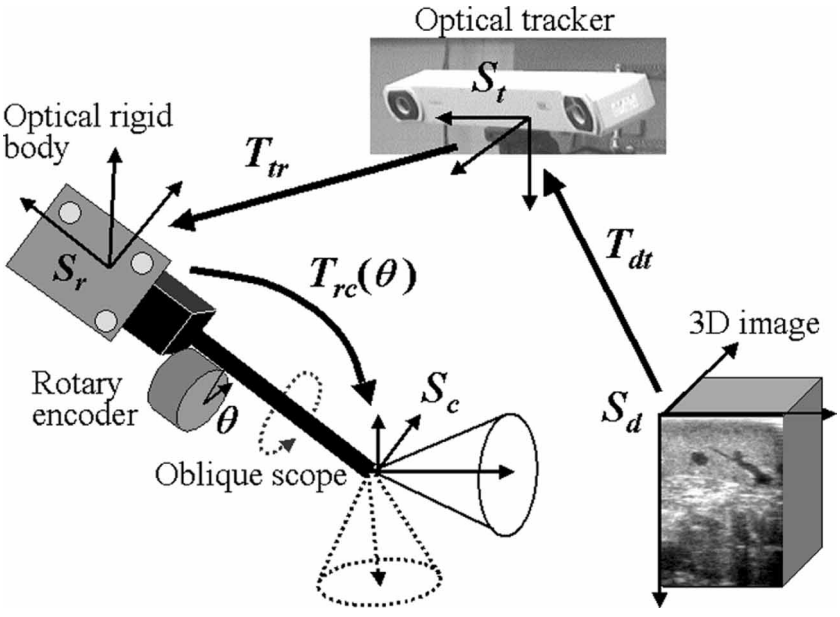

Figure 2. Basic system of oblique-viewing endoscopic augmented reality visualization.

where s is a scalar value, and $s = z_c$ when the z_c-axis of the camera coordinate system S_c is set as the optical axis. Intuitively, the procedures for obtaining T_{dt}, T_{tr}, T_{rc} and M_{ci} are regarded as registration between the physical space and 3D image data, camera tracking, calibration of the external camera parameters, and calibration of the internal camera parameters, respectively.

In this paper, we assume that T_{dt} can be found using an existing registration method. In addition, T_{tr} is measured using an optical tracker and P_{ci} is obtained using the conventional camera calibration method of Tsai. The parameters inherent in an oblique endoscope are included in T_{rc}. Let θ be the rotation parameter of the scope cylinder measured by the rotary encoder geared to it. The external camera parameters T_{rc} for oblique endoscopes are described as a function of θ, i.e., $T_{rc}(\theta)$. In the next subsection, we describe the modeling of $T_{rc}(\theta)$ for oblique endoscopes.

Camera model for oblique-viewing endoscope

Projection model of pinhole camera. In Tsai's calibration method, the camera parameters involved in the pinhole camera projection model are classified into external and internal parameters [7]. The external parameters determine the transformation from the world coordinate system S_w, which corresponds to S_r in Figure 2, to the camera coordinate system S_c. The internal parameters determine the projection of 3D points in the camera coordinate system onto the 2D image I_c. The camera parameters inherent in oblique scopes are mainly related to the external parameters. Let homogeneous coordinates of a 3D point in S_w be $\mathbf{p}_w = (x_w, y_w, z_w, 1)$, and those in S_c be $\mathbf{p}_c = (x_c, y_c, z_c, 1)$. Given the rigid transformation matrix T: $S_w \rightarrow S_c$, we have

$$\mathbf{p}_c = \mathbf{p}_w T, \tag{2}$$

where T corresponds to T_{rc} in Equation (1). Let I_c be the image coordinate system, and $\mathbf{i}_c = (u, v, 1)$ be homogeneous coordinates of the projected 2D point of $\mathbf{p}_c$ onto I_c. Given the image projection matrix M, we have

$$s\mathbf{i}_c = \mathbf{p}_c M = \mathbf{p}_w TM, \tag{3}$$

where M corresponds to M_{ci} in Equation (1), s is a scalar value, and $s = z_c$ since the z_c-axis is set as the optical axis. T in Equation (2) involves the external camera parameters, while M in Equation (3) involves the internal camera parameters, including the horizontal and vertical focal lengths, the horizontal and vertical pixel sizes, and the image center coordinates.

Simple camera model for idealized oblique-viewing endoscope

In the camera model for oblique scopes, we assume that the rotation angle θ of the scope cylinder is related to the external camera parameters T, but not to the internal camera parameters M. The rigid transformation matrix T representing the external parameters in Equation (3) is described as a function of the rotation angle θ of the scope cylinder, and is thus represented as $T(\theta)$.

Figure 3 shows a schematic diagram of the idealized camera model of oblique scopes. When the oblique scope is mathematically modeled as a pinhole camera, its camera coordinate system, (x_c, y_c, z_c), is virtually arranged as shown Figure 3. Here, it is necessary to carefully model the fact that, due to the rotation of the scope cylinder, only the lens system rotates while the camera head, i.e., the imaging plane, remains fixed irrespective of the rotation. We mathematically describe the transformation of the endoscopic image due to the rotation of the scope cylinder by decomposing the one physical rotation into two consecutive mathematical rotations. First, both the camera head (imaging plane) and cylinder are rotated as a single rigid body (we call this the *whole scope rotation*). Next, just the camera head is inversely rotated so that only the lens system (cylinder) rotates while the camera head remains fixed (we call this the *camera head rotation*).

In the whole scope rotation (Figure 3, left) the camera coordinate system S_c is rotated around the rotation axis l_s of the scope cylinder by θ. l_s ideally passes through the origin of S_c and intersects with the z-axis of S_c at a fixed angle φ_0, where φ_0 is the oblique viewing angle inherent in the oblique scope. The z-axis of S_c, i.e., the viewing direction, is rotated around l_s connected with the rotation θ of the scope cylinder, while the angle between l_s and the z-axis of S_c remains fixed at φ_0. By the whole scope rotation, the endoscopic image is changed from that in the left frame of Figure 3 to that in the center frame, where the counter-clockwise rotation of the dashed line shown below the "2" is observed.

The first whole scope rotation involves the movement of both the lens system and the imaging plane. Nevertheless, rotation of the imaging plane should not occur. Because the rotation of the camera head around l_s in the physical space virtually corresponds to the rotation of the imaging plane around the z-axis of S_c, the incorrect rotation of the imaging plane is nullified by the second camera head rotation of the xy-plane of S_c, because the horizontal and vertical axes of the imaging plane are aligned to the x- and y-axes of S_c. In the camera head rotation (Figure 3, center), the xy-plane of S_c is rotated by $-\theta$, i.e., inversely rotated, around

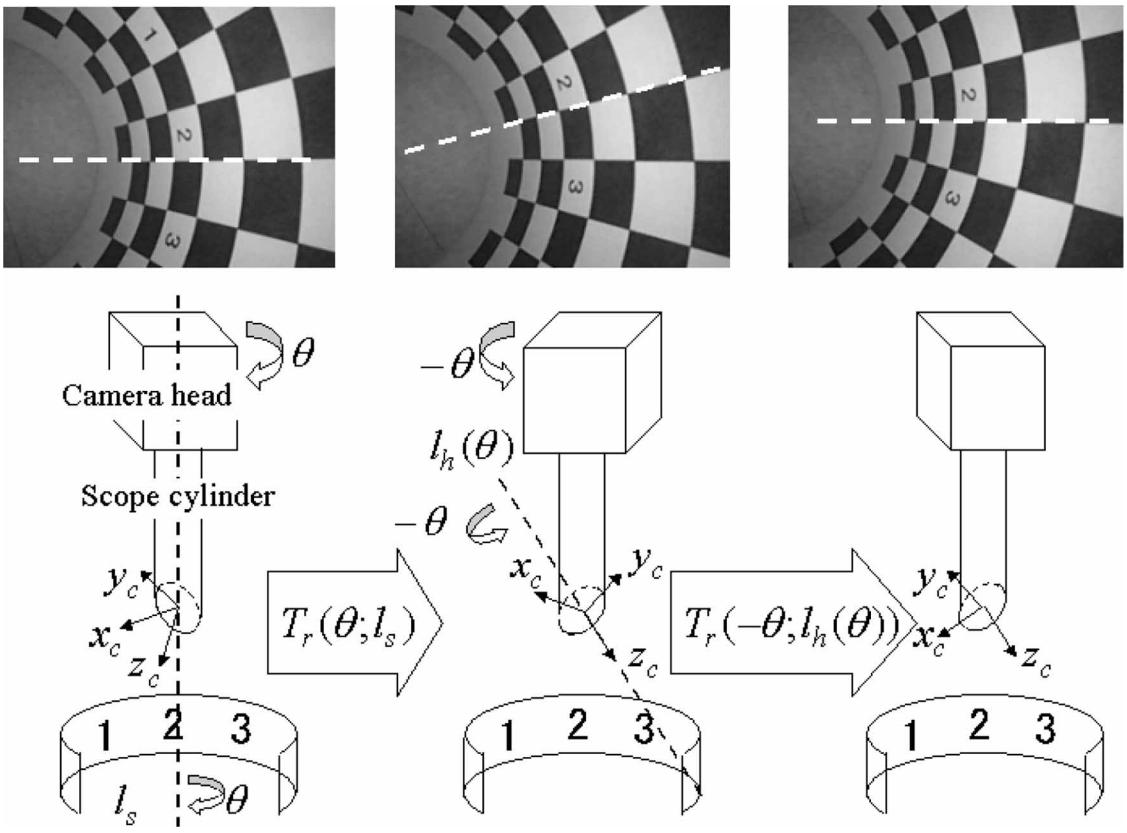

Figure 3. Schematic diagram of camera model for idealized oblique-viewing endoscope.

$l_h(\theta)$, which ideally corresponds to the z_c-axis of the camera coordinate system after the whole scope rotation of θ. Due to this inverse rotation, the view-up direction of the endoscopic image is returned to the original direction before executing the whole scope rotation. The endoscopic image is changed from that in the center frame of Figure 3 to that shown at the right of the figure, where the orientation of the dashed line below the "2" is aligned to the initial orientation. This is consistent with the characteristic of the oblique-viewing endoscopic image by which the view-up direction is invariant to the rotation of the scope cylinder.

We derive a mathematical description of $T(\theta)$ by combining the whole scope rotation and the camera head rotation in the following. Let $T_R(\theta; \mathbf{v}, \mathbf{x})$ or $T_R(\theta; l)$ be the transformation matrix representing the rotations θ around the axis l defined by point $\mathbf{x}$ and direction $\mathbf{v}$. Let $\mathbf{o}_c$ be the origin of S_c, and $\mathbf{n}_s$ be the direction of l_s (where $|\mathbf{n}_s| = 1$). Let $l_h(\theta)$ and $\mathbf{z}_c(\theta)$ be the z-axis of S_c, that is, l_h, and its direction, respectively, when the rotation angle of the scope cylinder is θ, that is, S_c is rotated by θ around l_s. Let T_0 represent the transformation matrix from S_w to S_c when $\theta = 0$, that is, when the scope cylinder is at zero rotation. T_0 is the rigid transformation representing the external parameters in Tsai's camera model when $\theta = 0$. When the scope cylinder is rotated by θ, the rigid transformation matrix representing the external parameters of the camera model for the ideal oblique scope, $T(\theta)$, can be given by

$$T(\theta) = T_0 T_R(\theta; l_s) T_R(-\theta; l_h(\theta)) \quad (4)$$

$$= T_0 T_R(\theta; \mathbf{m}, \mathbf{o}_c) T_R(-\theta; \mathbf{z}_c(\theta), \mathbf{o}_c), \quad (5)$$

where $T_R(-\theta; l_s)$ and $T_R(\theta; l_h(\theta))$ correspond to the whole scope rotation and the camera head rotation, respectively.

To simplify Equation (5), we rewrite the camera head rotation $T_R(-\theta; l_h(\theta))$ as

$$T_R(-\theta; l_h(\theta)) = T_R(-\theta; l_s) T_R(-\theta; l_h) T_R(\theta; l_s), \quad (6)$$

since the rotation around $l_h(\theta)$ is equivalent to the following three consecutive rotations: rotation around l_s by $-\theta$ to bring $l_h(\theta)$ to the initial pose l_h; rotation around l_h by $-\theta$ at the initial pose; and rotation around l_s by θ to bring l_h to $l_h(\theta)$, where it should be noted that $l_h = l_h(0)$. By combining Equations (5) and (6), $T(\theta)$ is written by rotations

around the fixed axes l_h and l_s:

$$T(\theta) = T_0 T_R(\theta; l_s) T_R(-\theta; l_h(\theta)) \quad (7)$$

$$= T_0 T_R(\theta; l_s)\{T_R(-\theta; l_s) T_R(-\theta; l_h) T_R(\theta; l_s)\} \quad (8)$$

$$= T_0 T_R(-\theta; l_h) T_R(\theta; l_s) \quad (9)$$

$$= T_0 T_R(-\theta; \mathbf{z}_c, \mathbf{o}_c) T_R(\theta; \mathbf{n}_s, \mathbf{o}_c). \quad (10)$$

Extended camera model for general oblique-viewing endoscope. Modeling of actual oblique scopes needs to incorporate deviations from the idealized model for accurate calibration. In the idealized model, several ideal situations are assumed. The following two violations of the assumptions are considered to seriously affect accuracy in calibration of actual oblique scopes:

- The origin of S_c does not pass through the axis l_s, where it is assumed that the direction of l_s is the same as that of the ideal model (Figure 4).
- In the camera head rotation, the rotation axis l_h of the xy-plane of S_c, i.e., the imaging plane, is deviated from the z-axis of S_c (Figure 5).

To address the first violation, we simply assume that l_s does not necessarily pass through $\mathbf{o}_c$ and that l_s is defined by point $\mathbf{c}_s$ and orientation $\mathbf{n}_s$.To address the second violation, we assume that l_h is described by unknown direction $\mathbf{n}_h$ and point $\mathbf{c}_h$ instead of by $\mathbf{z}_c$ and $\mathbf{o}_c$. By incorporating the above additional parameters, $T(\theta)$ is rewritten as

$$T(\theta) = T_0 T_R(-\theta; \mathbf{n}_h, \mathbf{c}_h) T_R(\theta; \mathbf{n}_s, \mathbf{c}_s). \quad (11)$$

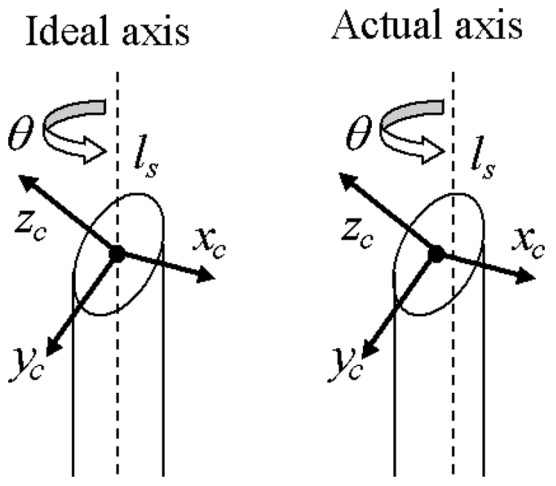

Figure 4. Modeling of rotation axis l_s in idealized model (left) and generalized model (right).

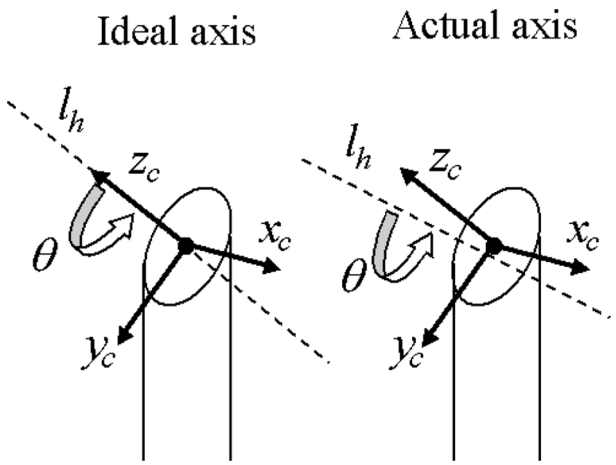

Figure 5. Modeling of rotation axis l_h in idealized model (left) and generalized model (right).

Calibration procedure

The camera calibration of oblique scopes involves the estimation of the following parameters:

- Rigid transformation T_0 from S_w to S_c at zero rotation of the scope cylinder, i.e., the external camera parameters of Tsai's model at zero rotation.
- Axis l_s, i.e., $\mathbf{n}_s$ and $\mathbf{c}_s$.
- Axis l_h at zero rotation of the scope cylinder, i.e., $\mathbf{n}_h$ and $\mathbf{c}_h$.

It is assumed that the determination of S_w and the measurement of θ are practically possible. In our experiments, we determined S_w by measuring 6D pose parameters of the optical rigid body attached to the camera head using an optical tracker, and measured θ using the rotary encoder geared to the scope cylinder.

The calibration procedure is as follows. First, T_0 is estimated when the rotation of the scope cylinder is fixed at $\theta = 0$. A projection matrix M representing the internal parameters is simultaneously estimated. This step is performed based on the conventional calibration procedure of Tsai. Next, l_s, that is, $\mathbf{n}_s$ and $\mathbf{c}_s$, is estimated by 3D measurement of the rotation of the scope cylinder itself. Finally, $\mathbf{n}_h$ and $\mathbf{c}_h$ are estimated using oblique endoscopic images acquired at several rotations θ of the scope cylinder, based on T_0, $\mathbf{n}_s$ and $\mathbf{c}_s$ as estimated during the first and second steps. In this step, θ^i was measured using a rotary encoder in our experiments. In the following subsections the second and third steps of the procedure are described in detail.

Estimation of l_s. To estimate $\mathbf{n}_s$ and $\mathbf{c}_s$ defining the axis l_s, we attach an optical marker to a knob for rotating the scope cylinder (as shown in Figure 6). The 3D

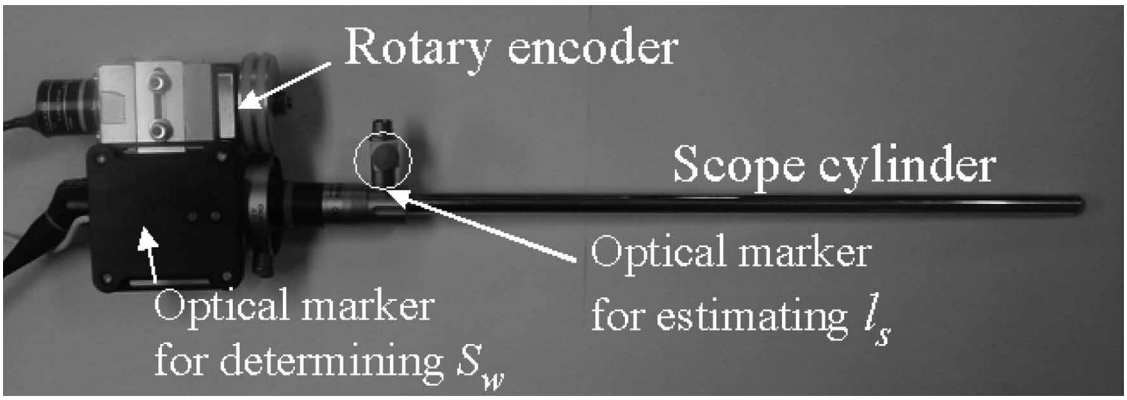

Figure 6. Oblique-viewing endoscope to which rotary encoder and optical makers are attached.

position of this optical marker during rotation of the scope cylinder is measured using an optical tracker. The camera head must be fixed while the cylinder is rotated. The normal of the plane fitted to the measured 3D positions is regarded as $\mathbf{n}_s$, and the center of the circle fitted to their trajectory is regarded as $\mathbf{c}_s$.

Let $\mathbf{r}_w^i$ $(i = 1, 2, \ldots, n)$ be the ith measured 3D position. $\mathbf{n}_s$ is estimated by finding the value of $\mathbf{n}_s$ minimizing

$$\sum_{i=1}^{n} \{\mathbf{n}_s \cdot \mathbf{r'}_w^i\}^2, \tag{12}$$

under the condition $|\mathbf{n}_s| = 1$, where $\mathbf{n}_s \cdot \mathbf{r'}_w^i$ denotes inner product and $\mathbf{r'}_w^i = \mathbf{r}_w^i - \bar{\mathbf{r}}_w$, in which $\bar{\mathbf{r}}_w$ is the gravity center of $\mathbf{r}_w^i$. Practically, $\mathbf{n}_s$ is estimated using the principal axis method by finding the eigenvector corresponding to the minimum eigenvalue of the 3×3 matrix $\sum_{i=1}^{m} \{\mathbf{r'}_w^i\}^t \cdot \mathbf{r'}_w^i$. Using the estimated $\mathbf{n}_s$, the center $\mathbf{c}_s$ of the circle fitting to $\mathbf{r'}_w^i$ is estimated. The square of the distance between $\mathbf{r}_w^i$ and axis l_s is given by $|\mathbf{r}_w^i - \mathbf{c}_s|^2 - (\mathbf{n}_s \cdot (\mathbf{r}_w^i - \mathbf{c}_s))^2$. Letting ρ be the radius of the fitted circle, $\mathbf{c}_s$ is estimated by finding values of $\mathbf{c}_s$ and ρ minimizing

$$\sum_{i=1}^{n} \{\rho^2 - |\mathbf{r}_w^i - \mathbf{c}_s|^2 + (\mathbf{n}_s \cdot (\mathbf{r}_w^i - \mathbf{c}_s))^2\}^2. \tag{13}$$

Note that ρ is not used in the camera model. This non-linear least square problem can be solved using the Levenberg-Marquardt method.

Estimation of l_h. To estimate $\mathbf{n}_h$ and $\mathbf{c}_h$ defining the axis l_h, we acquire endoscopic images at several rotation angles θ^i $(i = 1, 2, \ldots, m)$ of the scope cylinder. Let $\mathbf{i}_c^{ij}$ be the jth 2D point in the endoscopic image acquired at rotation angle θ^i, which is a projection of 3D position $\mathbf{p}_w^j$ in S_w $(j = 1, 2, \ldots, n)$. The relation between $\mathbf{i}_c^{ij}$ and $\mathbf{p}_w^j$ is described as

$$s\mathbf{i}_c^{ij} = \mathbf{p}_w^j T(\theta^i) M \tag{14}$$

where $s = z_c$, M is the projection matrix including the internal parameters, and $T(\theta^i)$ is the rigid transformation matrix including the external parameters for oblique scopes. The relation can be written as

$$\mathbf{i}_c^{ij} = \mathbf{p}_w^j T_0 T_R(-\theta^i; \mathbf{n}_h, \mathbf{c}_h) T_R(\theta^i; \mathbf{n}_s, \mathbf{c}_s) M. \tag{15}$$

Because M, T_0, $\mathbf{n}_s$ and $\mathbf{c}_s$ have already been estimated, only $\mathbf{n}_h$ and $\mathbf{c}_h$ are unknown in Equation (15). If we regard the right-hand side of Equation (15) as a function of $\mathbf{p}_w^j$ and θ^i, $\mathbf{i}_c$, whose range is projected in 2D coordinates, the relation can be written as

$$\mathbf{i}_c^{ij} = \mathbf{i}_c(\mathbf{p}_w^j, \theta^i; \mathbf{n}_h, \mathbf{c}_h). \tag{16}$$

That is, $\mathbf{n}_h$ and $\mathbf{c}_h$ are unknown system parameters in function $\mathbf{i}_c$. $\mathbf{n}_h$ and $\mathbf{c}_h$ are estimated by finding the values of $\mathbf{n}_h$ and $\mathbf{c}_h$ minimizing

$$\sum_{j=1}^{n} \sum_{i=1}^{m} |\mathbf{i}_c^{ij} - \mathbf{i}_c(\mathbf{p}_w^j, \theta^i; \mathbf{n}_h, \mathbf{c}_h)|^2. \tag{17}$$

This non-linear least square problem can be solved using the Levenberg-Marquardt method.

Results

Figure 6 shows the oblique scope with the additional apparatus used in the experiments. We used an OTV-S5C laparoscope (Olympus Optical Co. Ltd., Tokyo, Japan) as an oblique scope for evaluating the proposed camera model and calibration procedure. Since lens distortion was sufficiently small in this laparoscope, we did not apply any distortion

correction methods to the acquired endoscopic images. The rotary encoder geared to the scope cylinder was used for measuring the rotation angle θ of the scope cylinder. Its resolution was 0.25°. The Polaris (Northern Digital, Inc., Waterloo, Ontario, Canada) was used for all other 3D position measurements during the calibration processes.

Effects of estimation of l_s and l_h

Images of a checkerboard pattern were acquired using the oblique scope at different rotation angles of the scope cylinder within the range $0° \leq \theta \leq 132°$. The 3D positions $\mathbf{p}_w^j$ of the jth crossing point on the checkerboard in the world coordinate system S_w were measured using the Polaris pen-probe. The 2D coordinates $\mathbf{i}_c^{ij}$ of projection points corresponding to the jth crossing point were manually specified from the image (whose matrix size was 320×240) acquired at the ith rotation angle. Using the above data set for the calibration, l_h ($\mathbf{n}_h$ and $\mathbf{c}_h$) was estimated. Similarly, other data sets of $\mathbf{p}_w^j$ and $\mathbf{i}_c^{ij}$ were acquired for accuracy evaluation of the camera calibration through the different acquisition processes. Using the data sets for evaluation, we defined the projection error ε as

$$\epsilon = \frac{1}{mn} \sum_{i=1}^{m} \sum_{j=1}^{n} |\mathbf{i}_c^{ij} - \mathbf{i}_c(\mathbf{p}_w^j, \theta^i)| \quad \text{(pixels)}, \qquad (18)$$

where $\mathbf{i}_c(\mathbf{p}_w^j, \theta^i)$ denotes computed 2D coordinates using the calibrated parameters. It should be noted that ε is not residual because the data sets used for the calibration are different from those used for computation of ε. The numbers of angles θ^i, m, were $m = 8$ for the calibration data set and $m = 7$ for the evaluation data set. The seven angles at which the endoscopic images for evaluation were acquired were all different from those used for calibration. The number of manually specified 2D projection points, n, at each angle was $n = 16$ for both data sets.

We compared the respective errors ε of the following four calibration methods:

- Full calibration: All processes of the proposed method were applied.
- Calibration without estimation of l_h: T_0 and l_s were estimated, but l_h was not. Instead, l_h was assumed to correspond to the z-axis of S_c.
- Calibration without estimation of the position of l_s: T_0 was estimated, as was the direction of l_s, $\mathbf{n}_s$, but position $\mathbf{c}_s$ was not. Instead, l_s was assumed to pass through the origin of S_c. l_h was then estimated.
- Calibration without estimation of l_h or the position of l_s: The assumptions used in the preceding pair of methods were used instead.

Figure 7 shows the errors ε of the above four methods for different rotation angles, θ, of the scope cylinder. In the full calibration, ε was constantly low (around 2 pixels) irrespective of θ, but in the other calibration methods ε increased as θ increased, e.g., by more than 10 pixels when θ was greater than 75°. Figure 8 shows projection points computed using Equation (15) superimposed on the original images acquired at several angles for the evaluation data set. Results were compared between the full calibration and calibration without estimation of l_h. Significant improvements were observed in the full calibration. These results show that careful estimation of both l_h and l_s is quite important for accurate calibration.

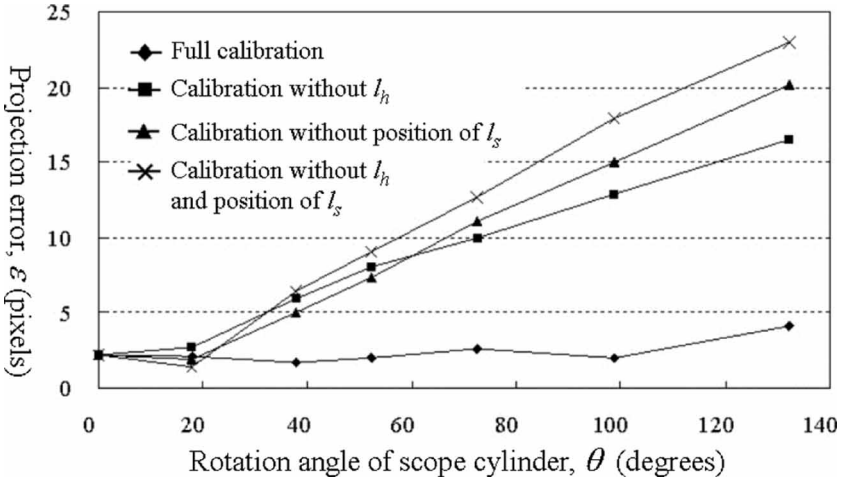

Figure 7. Relationship between the projection error, ε, (vertical axis) and the rotation angle of the scope cylinder, θ, (horizontal axis) in four different calibration methods.

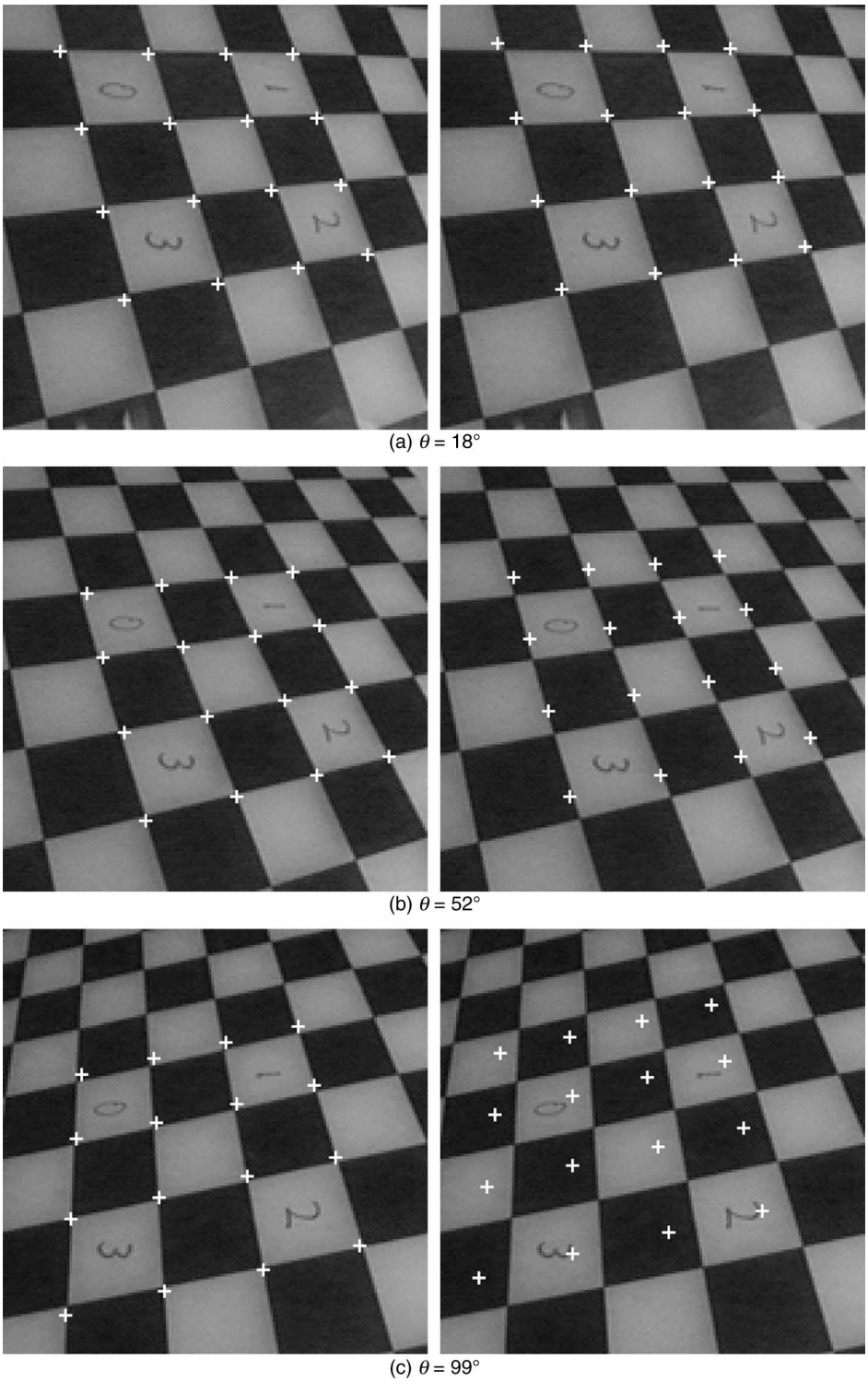

Figure 8. Computed projection points superimposed on original images. Left: full calibration estimating both l_s and l_h. Right: calibration without estimation of l_h (i.e., estimating only l_s). A 160 × 160 region was trimmed from the original 320 × 240 image. The size of each square of the checkerboard was 14 × 14 mm.

Effects of number of angles and point samples on estimation of l_h

When l_h is estimated, the number of angles θ^i, m, and the number of 3D points $\mathbf{p}_w^j$, n, projected onto the endoscopic image at each angle are considered to affect the accuracy of estimation of l_h. In the previous experiments, we used $m = 8$ for the range $0^\circ \leq \theta \leq 132^\circ$ and $n = 16$ for each angle of the endoscopic image. Evaluating the effects of the numbers of

θ^i and $\mathbf{p}_w^j$ is important to provide guidelines for efficient and accurate calibration. We evaluated the error ε under the following two conditions:

- Fixed angle number: The number of 3D points $\mathbf{p}_w^j$, n, was changed from $n = 1$ to $n = 16$ while the number of angles θ^i, m, was fixed at $m = 8$. Data sets used for calibration were extracted from the calibration data set used in the section entitled *Effects of estimation of l_s and l_h*. Sixteen 3D points as used in that section were labeled as shown in Figure 9a, and the 3D points were selected for each number of n as summarized in Table I.
- Fixed 3D point number: The number of angles θ^i, m, was changed from $m = 1$ to $m = 8$ while the number of 3D points $\mathbf{p}_w^j$, n, was fixed at $n = 2$ and $n = 4$. $n = 2$ and $n = 4$ were determined based on the experimental results with "fixed angle number". The angles θ^i were selected for each number of m as summarized in Table II.

In the above experiments, we used the same evaluation data set as used in the section headed *Effects of estimation of l_s and l_h* to evaluate the error ε.

Figure 9b shows the results when the number of angles θ^i, m, was fixed at $m = 8$. The error ε was not significantly different when $n \geq 2$. Thus, we performed the experiments with "fixed 3D point number" using $n = 2$ and $n = 4$. Figure 9c shows the results when the number of 3D points $\mathbf{p}_w^j$, n, was fixed at $n = 2$ and $n = 4$. When $n = 4$, ε was slightly reduced when m became large, although ε was not significantly different when $m \geq 4$. When $n = 2$, the error was larger for every value of m than when $n = 4$. When $n = 4$ and $m = 4$, ε was 2.4 (pixels). Even when $n = 2$ and $m = 1$, ε was 2.8 (pixels). By considering the fact that the error was 2.2 (pixels) when $\theta = 0$, where error in Tsai's calibration was involved but any error due to oblique scope calibration was not involved, additional error due to oblique scope calibration could become sufficiently small when $n = 4$ and $m = 4$.

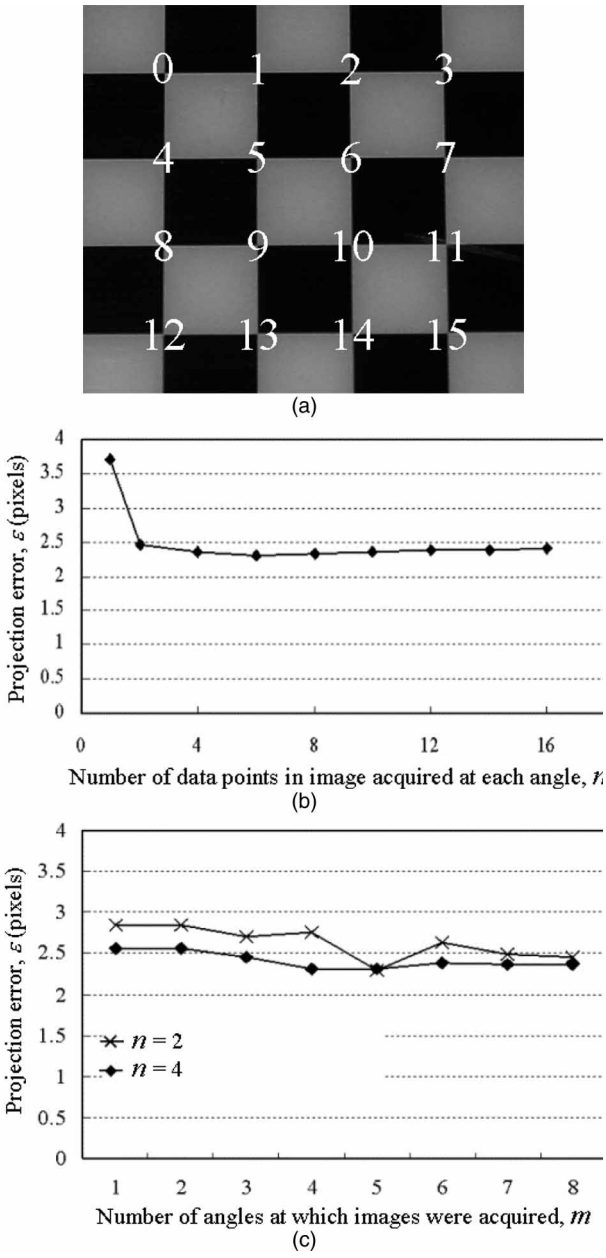

Figure 9. Effects of numbers of angles and sample points on estimation of l_h. (a) Labels of 3D points $\mathbf{p}_w^j$ for estimating l_h. (b) Relation between projection error, ε, and the number of sample points, n, when the number of angles was fixed at $m = 8$. (c) Relations between ε and the number of angles, m, when the number of 3D points was fixed at $n = 2$, 4.

Discussion and conclusions

We have developed the camera model and calibration procedure for oblique-viewing endoscopes. Both idealized and general models for oblique scopes have been formulated. In the calibration procedure of the general model, Tsai's calibration is performed at zero rotation of the scope cylinder, then the variation of the external parameters corresponding to the cylinder rotation is prescribed as a function of the rotation angle. A registration error of approximately two pixels was attained using our method. Accurate estimation of the rotational axes is included in the procedure. The results of the evaluations were proven to exert a significant effect on the overall calibration accuracy, especially when the rotation angle was large.

We measured the rotation angle θ of the scope cylinder using a rotary encoder. θ can also be measured using an optical or magnetic tracker by attaching an optical marker or magnetic receiver to the scope cylinder and linking the cylinder rotation to the marker or receiver motion. The rotary encoder was quite useful,

Table I. Conditions of 3D points $\mathbf{p}_w^j$ in experiments with fixed angle number.

No. of points, n	Point labels used for calibration (see Figure 9(a) for point labels)
1	9
2	0,15
4	0,3,12,15
6	0,3,5,10,12,15
8	0,3,5,6,9,10,12,15
10	0,3,4,5,6,9,10,11,12,15
12	0,2,3,4,5,6,9,10,11,12,13,15
14	0,2,3,4,5,6,7,8,9,10,11,12,13,15
16	0,1,2,3,4,5,6,7,8,9,10,11,12,13,14,15

however, since it was not subject to the line-of-sight requirement of an optical tracker or the magnetic field distortion of a magnetic tracker. Once the rotary encoder is geared so that cylinder rotation is directly linked to the rotary encoder, special attention for acquisition of θ is unnecessary.

In the results described in the section *Effects of estimation of l_s and l_h*, the overall accuracy was shown to be significantly affected by the estimation of l_s or l_h. When the cylinder rotation θ was larger than 30–40°, practical accuracy was not attainable without accurate estimation of both l_s and l_h. The error at $\theta = 0$ shown in Figure 7 was only due to Tsai's calibration procedure. The difference between this error and the average errors at other angles is considered to be additional error inherent in the oblique scope calibration procedure. The additional error due to the oblique scope calibration was less than 0.3 pixels, while the error at $\theta = 0$ due to Tsai's calibration was 2.2 pixels. This shows that the proposed calibration was quite effective.

In the experimental results described in the section *Effects of number of angles and point samples on estimation of l_h*, the effects of the number of acquired images with different θ and the number of 2D-3D point correspondences in each acquired image on estimation of l_h were evaluated. In the rotation angle range from 0 to 130°, good accuracy was attained by using images acquired at four angles and four points in each image. That is, 16 additional 2D-3D point correspondences were used in addition to Tsai's calibration at zero-rotation, and an error of 2.4 pixels was obtained, which was comparable to the error of 2.2 pixels only due to Tsai's calibration. Even when just two additional correspondences were used, that is, two correspondences in one image, the error of 2.8 pixels was attained. These results show that the proposed general camera model is quite suitable for describing the actual oblique-viewing scope.

Table II. Conditions of angles θ^i in experiments with fixed 3D point number.

No. of angles, m	Rotation angles of scope cylinder used for calibration (°)
1	132
2	132, 5
3	132, 50, 5
4	132, 85, 36, 5
5	132, 85, 36, 21, 5
6	132, 85, 50, 36, 21, 5
7	132, 85, 67, 50, 36, 21, 5
8	132, 221, 85, 67, 50, 36, 21, 5

Another possible approach to oblique scope calibration is to perform Tsai's calibration at a sufficiently large number of θ^i and interpolate each external parameter p^i estimated at θ^i. For example, in reference 12, camera parameters obtained at discrete values of the zoom and focus parameters using Tsai's calibration are interpolated using spline functions. Similarly, the external camera parameters involved in the cylinder rotation can be described as a continuous function of θ, $p(\theta)$, using spline functions from a discrete set of external parameter value p^i. At least six 2D-3D point correspondences are required in Tsai's method at each θ^i and additional correspondences are essential for stable calibration. While the accuracy of the above method would be largely affected by the number of angles θ^i at which Tsai's calibration is performed, our method is based on systematic descriptions of the mechanism of the oblique-viewing scopes, and thus good accuracy is attainable even with a small number of angles and correspondences.

In this paper, we used a laparoscope whose lens distortion was sufficiently small. However, quite a few endoscopes require the correction of lens distortion. We did not confirm whether the lens distortion correction and the calibration of oblique-viewing scopes can be independently applied, that is, whether the lens distortion parameters depend on the rotation angle θ. Future work will include analyzing this dependency and combining the lens distortion correction with the oblique scope calibration. Using the calibration method proposed in the present paper, we are now developing an augmented reality visualization system combined with intraoperating 3D ultrasound images [16, 17] for laparoscopic procedures using oblique scopes.

Acknowledgments

This work was partly supported by JSPS Research for the Future Program JSPS-RFTF99I00903.

References

1. Koppel D, Wang YF, Lee H. Automated image rectification in video-endoscopy. In: Niessen WJ, Viergever MA, editors. Proceedings of 4th International Conference on Medical Image

Computing and Computer-Assisted Intervention. (MICCAI 2001), Utrecht, The Netherlands, October 2001. Lecture Notes in Computer Science Vol 2208. Berlin: Springer, 2001. p 1412–14.
2. Helferty J, Zhang C, McLennan G, Higgins W. Videoendoscopic distortion correction and its application to virtual guidance of endoscopy. IEEE Trans Med Imag 2002;20:605–16.
3. Buck SD, Van Cleynenbreugel J, Geys I, Koninckx T, Koninck PR, Suetens P. A system to support laparoscopic surgery by augmented reality visualization. In: Niessen WJ, Viergever MA, editors. Proceedings of 4th International Conference on Medical Image Computing and Computer-Assisted Intervention. (MICCAI 2001), Utrecht, The Netherlands, October 2001. Lecture Notes in Computer Science Vol 2208. Berlin: Springer, 2001. p 691–8.
4. Khadem R, Bax MR, Johnson JA, Wilkinson EP, Shahidi R. Endoscope calibration and accuracy testing for 3D/2D image registration. In: Niessen WJ, Viergever MA, editors. Proceedings of 4th International Conference on Medical Image Computing and Computer-Assisted Intervention. (MICCAI 2001), Utrecht, The Netherlands, October 2001. Lecture Notes in Computer Science Vol 2208. Berlin: Springer, 2001. p 1361–5.
5. Shahidi R, Bax MR, Maurer CR Jr, Johnson JA, Wilkinson EP, Wang B, West JB, Citardi MJ, Manwaring KH, Khadem R. Implementation, calibration and accuracy testing of an image-enhanced endoscopy system. IEEE Trans Med Imag 2002;21:1524–35.
6. Stefansic JD, Herline AJ, Shyr Y, Chaman WC, Fitzpatrick JM, Dawant BM, Galloway RL. Registration of physical space to laparoscopic image space for use in minimally invasive hepatic surgery. IEEE Trans Med Imag 2000;20:1012–23.
7. Tsai RY. A versatile camera calibration technique for high-accuracy 3-D machine vision methodology using off-the-shelf TV cameras and lenses. IEEE J Robot Automat 1987;RA-3:323–44.
8. Haneishi H, Yagihashi Y, Miyake Y. A new method for distortion correction of electronic endoscope images. IEEE Trans Med Imag 1995;14:548–55.
9. Asari KV, Kumar S, Radhakrishnan D. A new approach for nonlinear distortion correction in endoscopic images based on least squares estimation. IEEE Trans Med Imag 1995;18:345–54.
10. Smith WE, Vakil N, Maislin SA. Correction of distortion in endoscopic images. IEEE Trans Med Imag 1992;11:117–22.
11. Dey D, Gobbi D, Slomka P, Surry KJM, Peters TM. Automatic fusion of freehand endoscopic brain images to three-dimensional surfaces: creating stereoscopic panoramas. IEEE Trans Med Imag 2002;21:23–30.
12. Willson RG. Modeling and calibration of automated zoom lenses. Ph.D. dissertation, The Robotics Institute, Carnegie Mellon University, Pittsburgh, PA, 1994.
13. Li MX, Lavest JM. Some aspects of zoom lens camera calibration. IEEE Trans Pattern Anal Machine Intell 1996;18:1105–10.
14. Edwards PJ, King AP, Maurer CR Jr, de Cunha DA, Hawkers DJ, Hill DLG, Gastion RP, Fenlon MR, Jusczyzck A, Strong AJ, Chandler CL, Gleeson MJ. Design and evaluation of a system for microscope-assisted guided interventions (MAGI). IEEE Trans Med Imag 2000;19:1082–93.
15. Yamaguchi T, Nakamoto M, Sato Y, Nakajima Y, Konishi K, Hashizume M, Nishii T, Sugano N, Yoshikawa H, Yonenobu K, Tamura S. Camera model and calibration procedure for oblique-viewing endoscope. In: Ellis RE, Peters TM, editors: Proceedings of 6th International Conference on Medical Image Computing and Computer-Assisted Intervention (MICCAI 2003), Montreal, Canada, November 2003, Part II. Lecture Notes in Computer Science Vol 2879. Berlin: Springer, 2003. p 373–81.
16. Sato Y, Nakamoto M, Tamaki Y, Sasama T, Sakita I, Nakajima Y, Tamura S, Monden M. Image guidance of breast cancer surgery using 3-D ultrasound images and augmented reality visualization. IEEE Trans Med Imag 1998;17(5):681–93.
17. Nakamoto M, Sato Y, Miyamoto M, Nakajima Y, Konishi K, Shimada M, Hashizume M, Tamura S. 3D ultrasound system using a magneto-optic hybrid tracker for augmented reality visualization in laparoscopic liver surgery. In: Dohi T, Kikinis R, editors. Proceedings of 5th International Conference on Medical Image Computing and Computer-Assisted Intervention (MICCAI 2002), Tokyo, Japan, September 2002, Part II. Lecture Notes in Computer Science Vol 2489. Berlin: Springer, 2002. p 148–55.